Piezoelectrically Transduced Temperature-Compensated Flexural-Mode Silicon Resonators

Vikram A. Thakar, *Student Member, IEEE*, Zhengzheng Wu, *Student Member, IEEE*, Adam Peczalski, *Student Member, IEEE*, and Mina Rais-Zadeh, *Senior Member, IEEE*

***Abstract*—In this paper, we explore the piezoelectric transduction of in-plane flexural-mode silicon resonators with a center frequency in the range of 1.3–1.6 MHz. A novel technique utilizing oxide-refilled trenches is implemented to achieve efficient temperature compensation. These trenches are encapsulated within the silicon resonator body so as to protect them during the device release process. By using this method, we demonstrate a high-Q ($> 19\,000$) resonator having a low temperature coefficient of frequency of < 2 ppm/°C and a turnover temperature of around 90 °C, ideally suited for use in an ovenized platform. Using electrostatic tuning, the temperature sensitivity of the resonator is compensated across a temperature range of $+50$ °C to $+85$ °C, demonstrating a frequency instability of less than 1 ppm. Using proportional feedback control on the applied electrostatic potential, the resonator frequency drift is reduced to less than 110 ppb during 1 h of continuous operation, indicating the ultimate stability that can be achieved for the resonator as a timing reference. The resonators show no visible distortion up to -1 dBm of input power, indicating their power handling capability. [2012-0261]**

***Index Terms*—Microelectromechanical systems (MEMS) resonators, oscillators, passive temperature compensation, piezoelectric resonators, power handling.**

I. Introduction

REPLACEMENT for quartz-based oscillators has been the focus of much research over the past two decades [1]–[3]. Silicon has been the main candidate for quartz replacement, and resonators made of silicon have been successfully commercialized for timing applications [4]–[6]. The literature reveals a number of articles on timing references investigating various designs and their corresponding electronic readout architectures. However, apart from a few exceptions [6]–[8], such designs have primarily focused on capacitive transduction, wherein the actuation gap is designed to be small for low motional impedance, consequently leading to power handling limitations [9]. Piezoelectrically transduced resonators are not limited by an actuation gap and can thus have excellent power handling capability [10]. In this work, we demonstrate aluminum nitride (AlN)-on-silicon flexural-mode resonators having a center frequency between 1.3 and 1.6 MHz and quality factors (Q) in the range of 19 000–25 000 with no visible distortion in the frequency response up to -1 dBm of input power.

In the case of timing references, the stability of the resonator with changing environmental conditions is of utmost importance. To address this concern, packaging technologies isolating the resonator from its environment have been proposed and subsequently commercialized [11]. Most resonator materials exhibit a large temperature coefficient of elasticity (TCE), which leads to significant temperature-induced frequency instability even inside the package. Thus, there is a need for temperature-compensated resonators through either material compensation or active frequency tuning [12], [13].

A common scheme for temperature compensation is the use of a material with a temperature coefficient of frequency (TCF) opposite to that of the main resonating material. For example, using a thermally grown oxide coating, which has a positive TCF, a silicon resonator (with a negative TCF) has been demonstrated with a frequency variation of less than 200 ppm over a wide temperature range [13]. In [13], the surface oxide was grown after device release in order to make the fabrication compatible with the final release process. In another work, a similar passive TCF compensation strategy utilizing oxide pillars uniformly distributed through the resonator has been demonstrated [14]. In this work, we implement oxide-refilled trenches entirely confined within the silicon resonator body to efficiently achieve a low TCF. As opposed to those in [14], the oxide-refilled trenches are not etched through the silicon layer, and thus, the compensating oxide is protected during the removal (i.e., through wet or dry etching) of the underlying buried oxide layer. We further show that the position of the oxide-refilled trenches in the resonator body, as seen in the schematic in Fig. 1, is critical toward maximizing temperature compensation with minimum material deposition and minimum Q degradation.

The underlying hypothesis of this work presumes that efficient temperature compensation of silicon resonators can be achieved by utilizing oxide-refilled trenches in areas of high strain energy density. Such a strategy has recently been demonstrated for temperature compensation of film bulk acoustic resonators [15]. In [15], a thin layer of silicon dioxide was deposited between two AlN layers to minimize the oxide required to achieve low resonator TCF. In this work, we analyze the strain profile for the case of flexural modes and implement

Manuscript received September 1, 2012; revised December 9, 2012; accepted January 17, 2013. This work was supported by the Defense Advanced Research Projects Agency under the Timing and Inertial Measurement Unit Program. Subject Editor D. Elata.

The authors are with the University of Michigan, Ann Arbor, MI 48109 USA (e-mail: thakar@umich.edu; zzwu@umich.edu; peczalsk@umich.edu; minar@umich.edu).

Color versions of one or more of the figures in this paper are available online at http://ieeexplore.ieee.org.

Digital Object Identifier 10.1109/JMEMS.2013.2245403

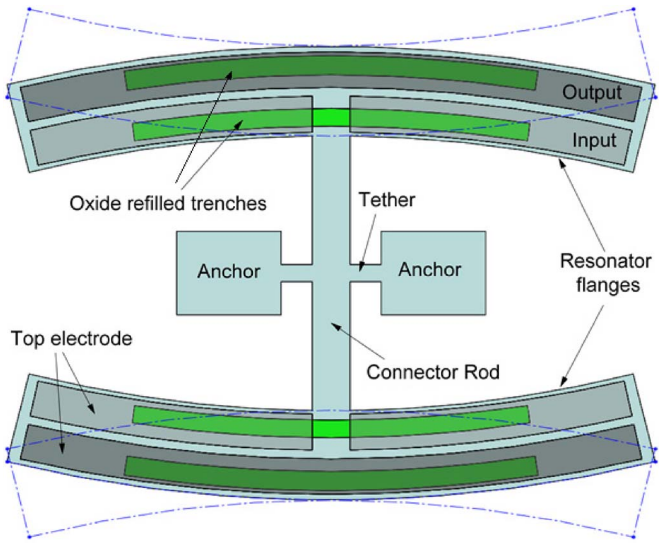

Fig. 1. Schematic view of the AlN-on-silicon resonator, showing the flexural mode of operation. The tuning electrodes are not shown in this schematic.

oxide-refilled trenches within the silicon resonator body to enable efficient temperature compensation while protecting these trenches during the resonator release. A detailed simulation study is undertaken to optimize the location of the trenches, and the results have been experimentally verified. While we demonstrate this compensation technique with piezoelectrically actuated resonators, the same method is also directly applicable to compensate electrostatically [9], [13] or thermally [16], [17] actuated resonators.

Active temperature compensation is still essential as passive compensation strategies are sensitive to fabrication-induced variations and can only compensate for the first-order TCE [13]. For fine control over the resonator center frequency, tuning through electrostatic spring softening is a commonly implemented strategy and is used in this work to demonstrate a compensated resonator across the temperature range of $+50$ °C to $+85$ °C, near its turnover temperature of $\sim$90 °C [18]. The frequency instability of the resonator with dc tuning is found to be within 1 ppm across this temperature range. In order to highlight the utility of such resonators in stable timing references, a proportional feedback control on the applied dc bias is implemented. By changing the applied dc bias as a function of the frequency error, the frequency drift is reduced to be better than 110 ppb, which indicates the timing stability that can be achieved with such resonators in temperature-controlled packages.

II. Fabrication

The fabrication process flow is presented in Fig. 2. The starting wafer is a 100-mm silicon-on-insulator wafer with a 20-μm-thick high-resistivity ($> 1000\ \Omega \cdot$ cm) device layer. In the first step, the temperature compensation trenches are etched using deep reactive-ion etching (DRIE) [Fig. 2(a)]. These trenches are subsequently refilled by growing 1.4 μm of thermal silicon dioxide at 1200 °C. It should be noted that the trench depth is kept slightly less than the device layer thickness to ensure that there is silicon separating the buried oxide layer from the oxide-refilled trenches. Postoxidation, the

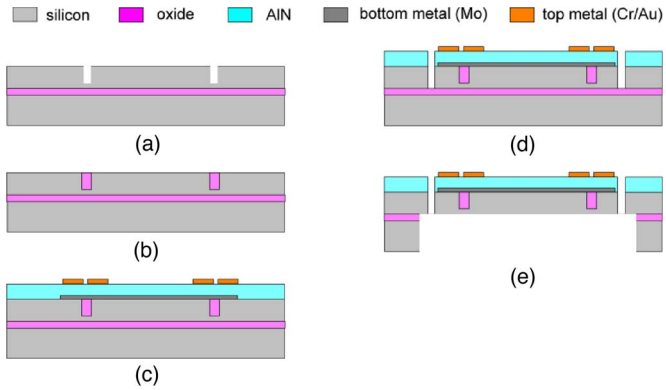

Fig. 2. Fabrication process flow of the AlN-on-silicon flexural-mode resonators. (a) Etch TCF compensation trenches. (b) Grow thermal oxide to refill trenches. Polish the wafer to get a flat substrate. (c) Deposit and pattern 100-nm bottom metal (Mo). Sputter a 0.5-μm-thick AlN film. Evaporate the top metal 100 nm thick. (d) Etch the release trenches in AlN and the silicon device layer. (e) Release the resonator using backside DRIE. Etch the buried oxide layer using RIE.

wafer surface is polished to a smooth and flat finish using an IPEC-472 [19] chemical–mechanical polishing (CMP) tool [Fig. 2(b)]. A smooth surface is essential for the reactive sputtering of high-quality AlN with low stress and vertical c-axis orientation. After CMP, 100-nm-thick molybdenum (Mo) is deposited as the bottom electrode. The Mo layer is patterned to reduce eddy currents during AlN sputtering which enables better control of the AlN film stress. A 0.5-μm-thick low-stress AlN transduction layer is subsequently deposited in a Tegal AMS SMT reactive sputtering system. A 100-nm-thick gold (Au) layer is evaporated and lift-off patterned as the top metal. A thin chromium (Cr) layer (10 nm) is used to improve adhesion between Au and AlN [Fig. 2(c)]. The gap between the resonator and the tuning electrodes is defined by etching the AlN and the silicon device layer using DRIE [Fig. 2(d)]. Finally, the device is released by selective backside removal of silicon and the buried oxide layer [Fig. 1(e)].

In order to demonstrate the applicability of this compensation strategy with wet release, proof-of-concept devices have been fabricated. In this case, a slightly modified fabrication process was implemented. After the trench refill process [Fig. 2(b)], a 2-μm-thick polysilicon layer was deposited and subsequently polished in order to protect the oxide-refilled trenches during wet release. The rest of the process up to that in Fig. 2(d) remained the same. In the final step, the devices were released using a $1:1$ 49% HF:DI water solution. Native oxide on the polysilicon surface was removed with a short HF dip before bottom electrode deposition to prevent Mo lift-off during the release. Fig. 3 shows the scanning electron microscope (SEM) images of a fabricated resonator.

III. Theory and Device Design

The device is designed in an IBAR configuration [20] composed of a central rod holding the resonating flanges and anchored to the substrate through small tethers (Fig. 3). This device configuration has been previously explored in great detail and has been proven to provide high-Q resonators with a large electrostatic tuning range [20], [21]. A piezoelectric actuation scheme is implemented in this work to improve the

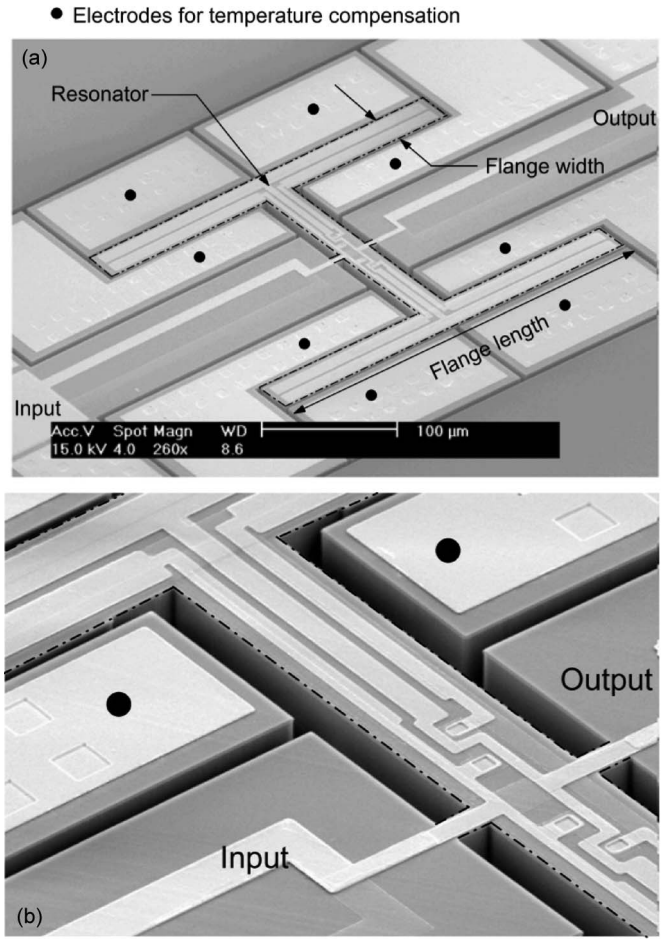

Fig. 3. (a) SEM image of a fabricated resonator. There are a total of eight tuning electrodes, which can be used for tuning the center frequency. (b) Close-up view showing the metal routing on the central rod. The black line (dashed–dotted) marks the outline of the resonator body.

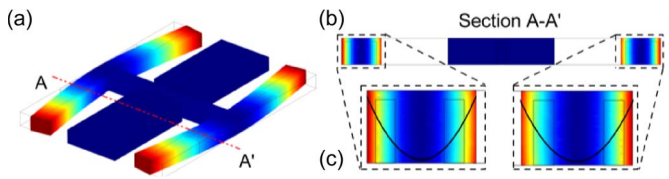

Fig. 4. (a) Simulated mode shape and (b) simulated strain energy density along section A–A′. (c) Close-up view of the strain energy density variation across the resonator flange cross section. The overlaid parabolic curve (in black) represents the variation of the strain across the width of the resonator flange. The color spectrum in (a) plots the total displacement, and those in (b) and (c) plot the strain energy density. Refer to Fig. 6 for the relative magnitude of the strain energy across the cross section.

power handling of the resonators while maintaining a high Q. The choice of using a single connector rod was made as opposed to the designs in [20] to allow for a simpler electrode layout required for piezoelectric actuation. The resonator is designed for operation in the first-order flexural mode for which the resonance frequency can be approximated as

$$f \cong 0.646 \frac{w}{L^2} \sqrt{\frac{E}{\rho}}. \tag{1}$$

An explanation of the terms is given in the Appendix. Fig. 4(a) plots the mode shape of the first-order flexural resonance mode. Fig. 4(b) plots the strain energy density across the cross section marked in Fig. 4(a). From these simulation results, we can find areas of high strain for the mode of interest. As shown in Fig. 4, the regions of high stress are near the device edges in the case of flexural modes. By placing oxide-refilled trenches close to the resonator edge, where strain energy is high, efficient temperature compensation can be achieved. To verify this, simulations were performed with a specific oxide-refilled trench size but located at different regions across the resonator flange width. Fig. 5 shows the location of trench pairs used in this study, and Fig. 6 plots the results obtained from the simulations.

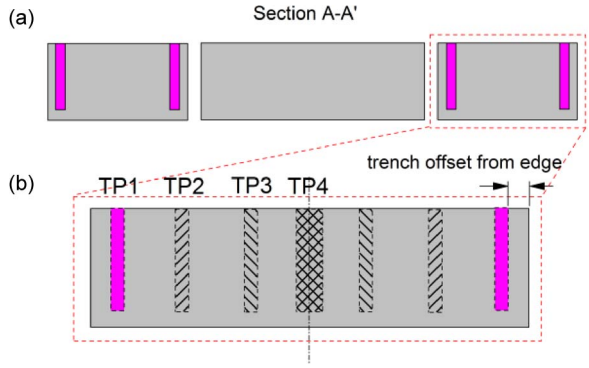

Fig. 5. Location of oxide-refilled trenches within the resonator (not to scale). Trenches with similar hatch/fill patterns form a trench pair.

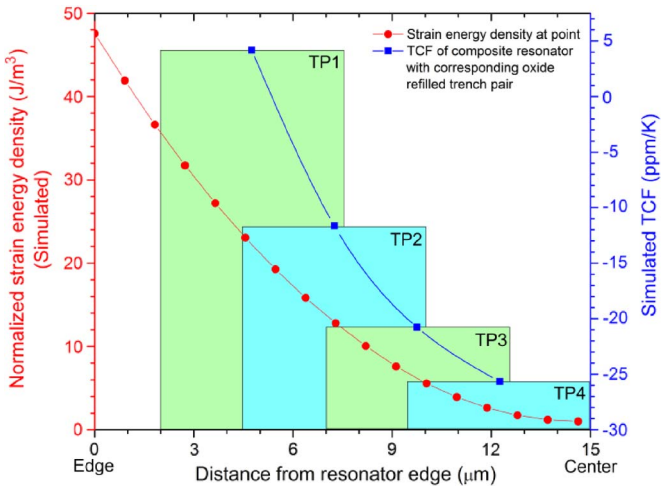

Fig. 6. Plot showing the variation in strain energy density (normalized) across the width of the resonator. Only one-half of the flange width is shown here. The TCF of the composite resonator is plotted as a function of the trench location. A clear correlation between the strain energy across the trench and the resonator TCF can be observed. In all cases, the width of the oxide-refilled trenches is 5.5 μm, and the total volume of the oxide is the same.

The simulated strain energy density across the resonator width is plotted on the left y-axis (red curve) in Fig. 6. The simulated TCF of the resonator as a function of the trench location is plotted on the right y-axis (blue curve). The physical location of the oxide-refilled trenches within the device is noted on the x-axis, which represents the flange width from its edge to the center. The volume of the compensation material (silicon dioxide) taken in each simulation is the same. The height of the trenches in Fig. 6 correlates to the simulated TCF, while their width correlates with the physical location of the trenches within the resonator. The material properties used in the TCF

TABLE I
MATERIAL PROPERTIES USED IN THE TCF SIMULATIONS (ALL VALUES ARE AT 25 °C)

	E (GPa)	TCE (ppm/K)	α (ppm/K)
Silicon	169	-64	+2.6
Oxide	71	+187.5	+0.5

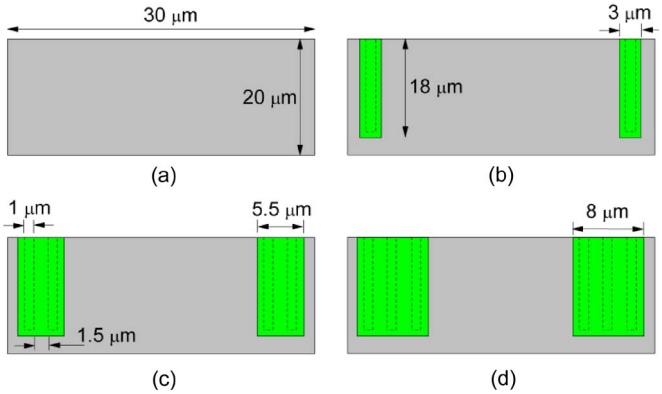

Fig. 7. Different trench configurations used in the characterization study. All trenches have the same dimensions and are shown with dotted lines. The spacing between the two etched trenches is kept as 1.5 μm (as marked) in order to ensure that the trenches are fully refilled with thermal oxide.

TABLE II
SIMULATED TCF VALUES AT 25 °C FOR THE FOUR RESONATOR CONFIGURATIONS SHOWN IN FIG. 7

Configuration	TCF	Configuration	TCF
No oxide	-30 ppm/°C	2 trenches	-2 ppm/°C
1 trench	-14.9 ppm/°C	3 trenches	4.3 ppm/°C

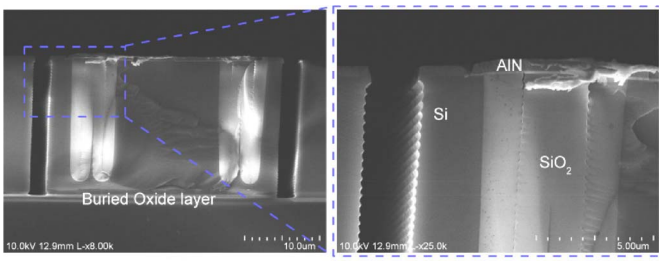

Fig. 8. Cross-sectional SEM images showing the oxide-refilled trenches for a two-trench sample. The close-up view on the right reveals small air pockets formed during the refill process.

simulations are summarized in Table I. From the results in Fig. 6, a strong correlation between the strain energy within the oxide-refilled trench area and the compensated TCF of the resonator can be observed.

Based on the optimization results, the four configurations shown in Fig. 7 have been experimentally investigated in this work. While all configurations have different oxide-refilled trench widths, the trenches are at the same distance from the resonator edge, and thus, they are expected to result in different TCF values. Table II summarizes the simulated TCF values for the four configurations in Fig. 7. For the three-trench configuration, the total strain energy in the trenches is $\sim$35% of the total energy of the mode, while its volume is less than 10% of that of the whole resonator.

Fig. 8 shows a cross-sectional image revealing the quality of the trench refill process. To allow for fabrication tolerances, a 2-μm offset from the resonator edge is maintained in the fabricated designs.

TABLE III
RESONATOR GEOMETRY USED FOR THE EXPERIMENTAL TCF CHARACTERIZATION

Parameter	Dimension (µm)	Parameter	Dimension (µm)
Flange length (L)	320	Tether length (L_t)	7.5
Flange width (w)	30	Tether width (w_t)	6
Rod length (L_R)	180	Si device thickness (t_{Si})	20
Rod width (w_R)	25	AlN thickness (t_{AlN})	0.5

TABLE IV
CONTRIBUTION OF DIFFERENT LOSS MECHANISMS ON THE Q AT 25 °C. THE SIMULATED Q_{Anchor} FOR THE COMPENSATED STRUCTURE ASSUMES IDEAL GEOMETRY WITH RECTANGULAR REFILLED TRENCHES

	Q_{TED} (simulated)	Q_{Anchor} (simulated)	Q_{Total} (simulated)	Q_{Total} (measured)
No T	31,890	180,000	~27,090	25,000
T1	31,915	180,000	~27,110	21,000
T2	31,410	180,000	~26,740	20,000
T3	32,575	180,000	~27,580	19,000

A. Resonator Quality Factor

The device is designed such that the 20-μm-thick silicon layer is actuated with only a thin layer of AlN (500 nm). The resonator layout and the AlN thickness are optimized for reduced anchor loss using simulations based on the theory presented in [22]. An anchor Q of $\sim$180 000 was simulated for the device shown in Fig. 3. The device dimensions are presented for reference in Table III.

A device operating around the design frequency of 1.5 MHz is expected to have its Q limited by thermoelastic damping (TED) when operated in vacuum. Q_{TED} is simulated to be $\sim$32 000 for the uncompensated structure using the method outlined in [23]. Table IV summarizes the contribution of different loss mechanisms on the Q of the resonator. While we expect the inclusion of oxide-refilled trenches to improve Q_{TED} (due to the significantly lower thermal conductivity of the oxide) [24], the simulated results in Table IV seem to suggest otherwise. The presence of AlN, which has a high thermal conductivity of 284 $\mathrm{W \cdot m^{-1} \cdot K^{-1}}$, offsets the benefit obtained from the oxide-refilled trenches, leading to no net improvement in the simulated Q_{TED}. It should be noted that, in these simulations, the effect of air damping and the fabrication-induced geometric variations have been ignored.

B. Active Temperature Compensation

From the simulation study, it is clear that the resonator TCF is a function of the trench location. Alignment tolerances during fabrication can thus cause uncertainty in the actual resonator TCF. In addition, while passive techniques can compensate for the first-order TCE, the higher order TCE terms remain uncompensated, and active compensation techniques are essential to achieve a temperature-stable performance [13].

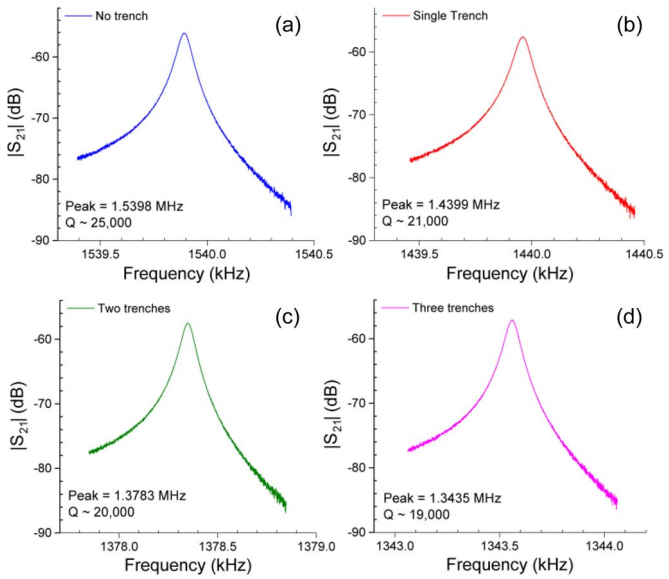

Fig. 9. Measured response of the resonators with (a) no TCF compensation, (b) single oxide-refilled trench, (c) two oxide-refilled trenches, and (d) three oxide-refilled trenches. All measurements are taken in vacuum and at room temperature.

Tuning of the resonance frequency by applying a dc bias to the resonator relative to the ground electrode is commonly used, and frequency tuning as large as -7.92 ppm/V^2 has been demonstrated for capacitively transduced resonators [20]. In this work, we employ the same dc tuning technique (also known as the spring softening method) for the piezoelectrically actuated resonators to compensate for the residual TCF terms and achieve frequency stability better than 1 ppm over a broad temperature range.

Using energy methods, the following equation for the resonator center frequency with applied dc bias, operated at the first-order flexural mode, can be derived (refer to the Appendix for the derivation and explanation of terms):

$$f = \frac{1}{2\pi} \cdot \sqrt[2]{\left[\frac{4}{3}\frac{E}{\rho}w^2 \cdot \frac{z_1^4}{L^4} - \frac{n_1 n_2}{8}\frac{\epsilon}{\rho} \cdot \frac{1}{w \cdot d^3} \cdot V^2\right]}. \quad (2)$$

This relation can be used to actively compensate the temperature-induced frequency variations.

IV. Measurements and Analysis

In order to characterize the performance of the devices, measurements are carried out using an Agilent E5061B network analyzer in an enclosed chamber at a vacuum level of $\sim$10 μtorr.

Fig. 9 shows the measured results for the devices with different oxide-refilled trench sizes as shown in Fig. 7. From the analysis of loss mechanisms, the resonator Q was found to be limited by TED. With the addition of oxide-refilled trenches, the device Q was expected to marginally improve as the thermal conductivity of the oxide is significantly lower than that of silicon [24]. From the simulated Q_{TED} given in Table IV, it was seen that the presence of AlN works to offset any improvement in the Q_{TED} and the device Q remained independent of the number of trenches. However, the measured results show a small Q drop as the number of trenches is increased. From the cross-sectional images [Fig. 8(b)], small air pockets can be seen as a consequence of the trench refill process. The number of lines of air pockets (voids) corresponds to the number of trenches refilled. These voids, along with the higher stress in the devices with larger volume of oxide, may be responsible for the measured Q degradation. Second, any misalignment in the location of the trenches with respect to the resonator edge can also degrade the anchor Q, consequently leading to a reduction in the measured Q. A maximum Q degradation of 24% is measured for the device with three trenches.

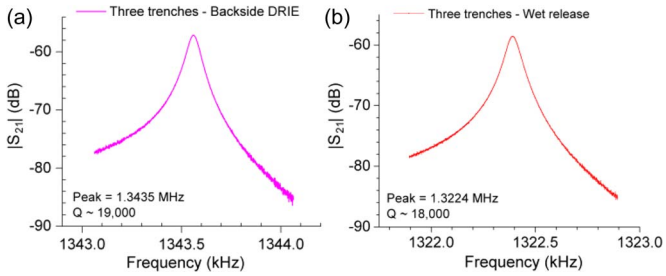

Fig. 10. Measured response of two resonators fabricated using (a) dry (backside DRIE) and (b) wet (HF) release processes.

TABLE V
Comparison of Measurement Results for Dry- and Wet-Released Samples

# of trenches	Wet release		Dry Release	
	f_0 (MHz)	Q	f_0 (MHz)	Q
0	1.5333	23,000	1.5398	25,000
1	-	-	1.4399	21,000
2	1.3564	18,805	1.3783	20,000
3	1.3224	18,140	1.3435	19,000

In order to verify process compatibility with wet release processes, proof-of-concept devices have been fabricated using HF release. Fig. 10 plots the measured response of two resonators released using dry and wet processes. The two devices are seen to show comparable results. It should be noted that the addition of the polysilicon layer in the wet-released samples does not significantly affect the in-plane flexural-mode frequency. Table V shows the comparison of the measured results from the dry- and wet-released samples.

A. Passive Temperature Compensation

In order to characterize the temperature dependence of resonance frequency, devices are measured in a Lakeshore cryogenic probe station. Backside-released samples have been used for this study due to their higher process yield in an academic clean room.

The temperature stability of the devices was characterized between -40 °C and $+85$ °C, and the results are shown in Fig. 11. The measured results compare well with the simulated values summarized in Table II. In order to compare the performances of the devices with different trench configurations, their relative frequency shift (in parts per million) is plotted as a function of temperature in Fig. 12. The two- and three-trench configurations show the lowest variation (< 500 ppm) over the temperature range of -40 °C to $+85$ °C.

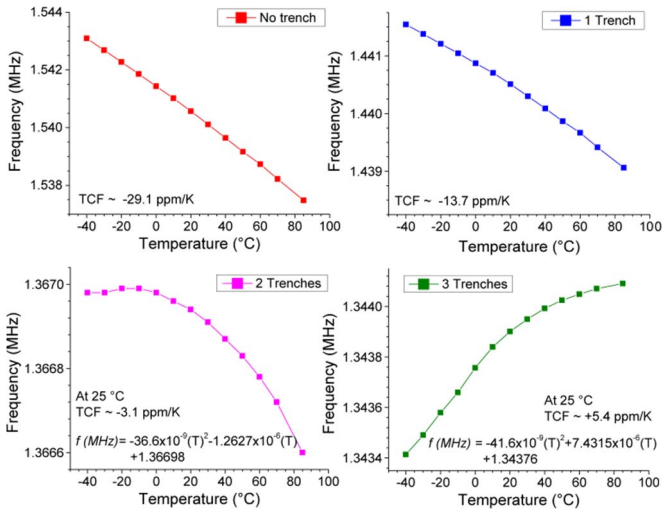

Fig. 11. Measured resonance frequency as a function of temperature for different trench configurations. In the case of the no- and single-trench resonators, the TCF value is averaged across the temperature range. For the case of the two- and three-trench devices, the TCF value is at 25 °C. The equation of the fitted second-order polynomial has also been included.

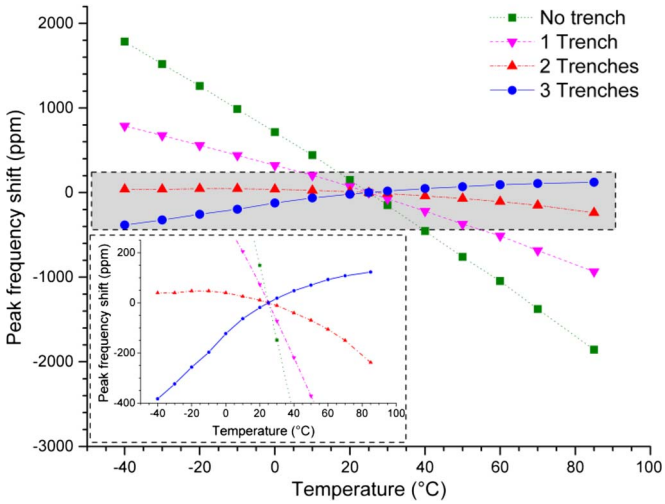

Fig. 12. Measured peak frequency shift in parts per million with temperature for different trench configurations. (Inset) Measured results in a smaller range.

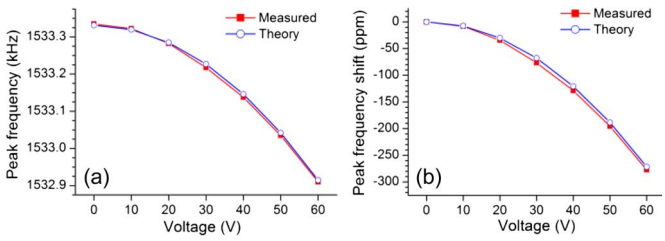

Fig. 13. Measured and calculated frequency tuning as a function of the applied dc voltage for a trenchless device. (a) Change in peak frequency and (b) total frequency tuning in parts per million.

B. Active Temperature Compensation

As shown in Fig. 2, the device has eight separate pads for active temperature compensation. Using all available electrodes, a total tuning range of 425 Hz is possible with an applied voltage of 60 V (Fig. 13). The expected frequency change calculated using (2) is also plotted in Fig. 13 for comparison.

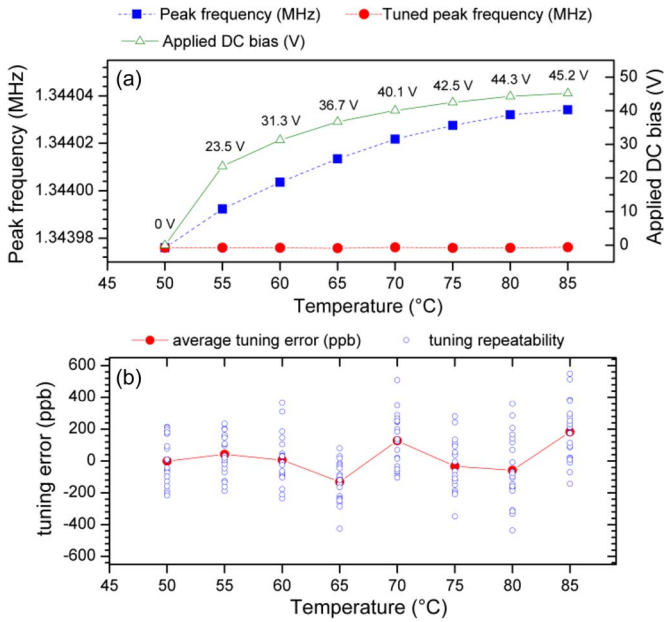

Fig. 14. (a) Measured frequency change with temperature for a three-trench device. The tuned frequency with applied dc voltage is also plotted to demonstrate the viability of this approach in achieving temperature-stable resonators. (b) Tuned peak frequency as a function of temperature and voltage. The graph details the tuning error for multiple measurements (total 20 readings at each temperature) at each voltage setting and the average value. The tuning error is within 1 ppm and is set by power supply fluctuations, resonator drift, and the stability of the temperature controller.

The low tuning sensitivity of -0.125 Hz/V^2 extracted from Fig. 13 can be attributed to the relatively large gap between the resonator body and the tuning electrodes ($\sim$2 μm). The lower tuning sensitivity has the advantage of relaxing the stability requirement on the bias voltage (reduce the frequency jitter due to supply voltage noise). Fig. 14 shows the result of the electrostatic tuning of the three-trench resonator across the temperature range of $+50$ °C to $+85$ °C using a single tuning electrode. To obtain the data in Fig. 14, the reference temperature was chosen to be $+50$ °C (since the device has positive TCF). As the temperature is increased, the frequency increases due to the resonator TCF. A corresponding dc bias voltage, calculated from the frequency–voltage curve at that temperature, was then applied at each temperature reading to tune the center frequency back to that at the reference temperature. Multiple readings were recorded at each temperature and voltage setting to look at the stability of tuning. The overall tuning accuracy is seen to be within 1 ppm. It should be noted that only a single tuning electrode was used to compensate the temperature-induced frequency drift for this measurement.

C. Resonator Drift Compensation

From the tuning stability results in Fig. 14, it is clear that the resonator short-term drift is on the order of a few hundred parts per billion. Likely causes include temperature drift, power supply fluctuations, and the intrinsic resonator drift. In order to provide an estimate of the resonator intrinsic drift, a compensation scheme is implemented to keep the resonator center frequency constant by changing the applied dc bias in a feedback loop.

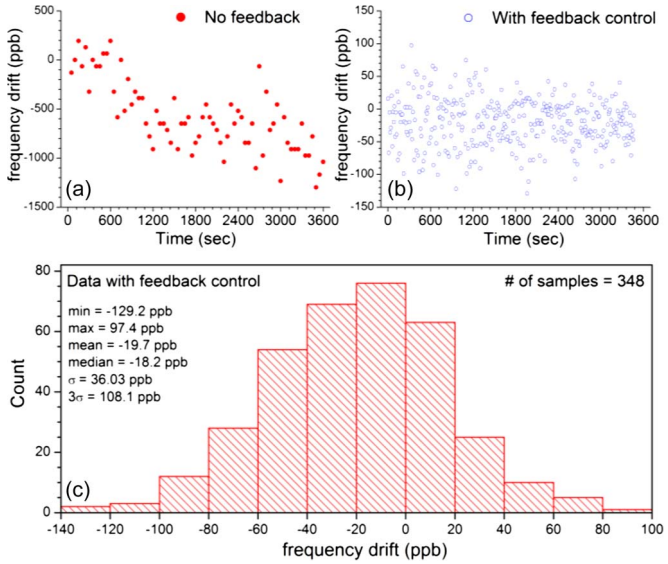

Fig. 15. Measured drift of the resonator center frequency (a) without and (b) with a feedback control loop. (c) Histogram plot of the resonator center frequency with feedback control showing the calculated statistical parameters assuming a Gaussian distribution. The resonator intrinsic drift is seen to be better than 110 ppb (3σ number).

With this technique, any drift effects can be reduced, leading to a more frequency-stable resonator performance. Thus, the measured variation, with the applied compensation, provides a rough estimate of the resonator intrinsic drift. Fig. 15 shows the measured results for the same device obtained with and without frequency compensation. The feedback algorithm is implemented using LabVIEW (National Instruments, Austin, TX, USA) [25] with the error signal calculated as the difference between the measured frequency and the reference frequency. The starting dc bias is taken to be 50 V, and a proportional feedback correction is applied with a resolution of 0.1 V. These measurements are carried out at room temperature in vacuum. The histogram of the measurement data is also plotted for reference. From the results, the standard deviation (σ) for the center frequency shift is calculated to be 36 ppb and demonstrates the improved resonator stability possible with appropriate drift compensation techniques. It should be noted that this σ is a conservative estimate and can be further improved either by optimizing the feedback control implementation or by compensating out any correlated drift effects through the use of multiple resonators.

D. Power Handling

A major advantage of using piezoelectric transduction over capacitive actuation is the improvement in power handling. Electrostatic resonators are usually designed to have very small actuation gaps, leading to significant nonlinearity at high ac input power levels. Piezoelectric resonators, on the other hand, do not have such limitations and can be designed for higher power handling and linearity limits. Fig. 16 shows the measured response of a resonator for input powers of -20 and -1 dBm. No distortion is seen in the resonator response, indicating good power handling capability. At 0-dBm input power (inset), nonlinear operation can be seen.

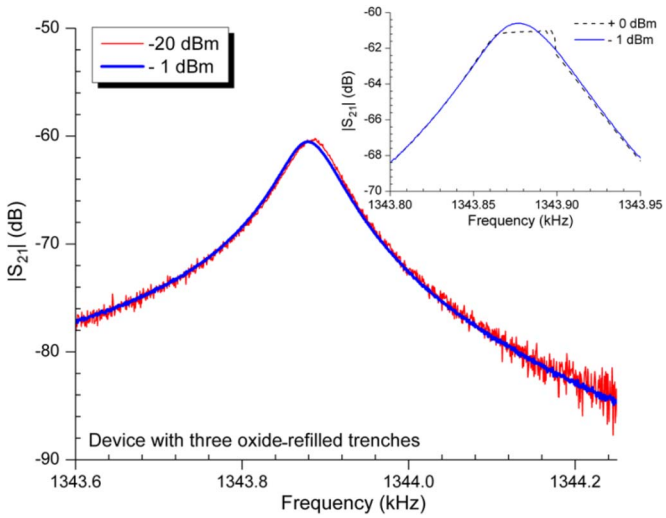

Fig. 16. Measured response of a resonator having three oxide-refilled trenches at different input power levels. There is no visible distortion up to -1 dBm of input power. The frequency shift can be attributed to the piezoelectric spring softening effect. The inset shows the distortion seen at 0-dBm power input, indicating the power handling limit of the device.

V. Discussion

For low-power and stable timing references, a resonator should possess a high quality factor, a low motional impedance, and a low temperature-induced drift. While the oxide-refilled trenches within the resonator body enable us to achieve the desired temperature dependence around the ovenization temperature, the motional impedance and the device Q can be further optimized.

As seen from the simulations, the cause of the Q limit in the presented resonators is identified as TED. Thus, design modifications leading to reduced TED should provide a higher device Q. One approach could be to pattern the AlN layer and co-optimize the location of the oxide-refilled trenches for both temperature compensation and an improved Q_{TED}, along the lines of previous work with air voids [24]. This will allow maintaining similar operating frequencies with better device performance without compromising on the electrostatic tuning coefficient.

The motional impedance of piezoelectric resonators is defined by both the electrode area and its location on the device. The main cause of the large motional impedance in the presented devices can be attributed to the position of the electrodes. If both electrodes and AlN were deposited along the device sidewall, it would significantly improve the insertion loss of the resonator. An example of such a process has been recently demonstrated [26].

While passive temperature compensation strategies can significantly reduce temperature-induced frequency variations, active tuning is essential to meet the stringent stability requirements of timing references. In the case of electrostatic tuning, applying dc bias can only be used to reduce the center frequency. As a result, nominal operation requires a nonzero dc bias, leading to unnecessary power consumption via leakage currents. An active compensation scheme allowing resonance frequency tuning in both directions will be extremely beneficial for resonator application in low-power timing references.

VI. Conclusion

In this paper, we have demonstrated effective TCF compensation of silicon resonators by positioning oxide-refilled trenches in regions of high strain. We showed a temperature-compensated piezoelectrically actuated flexural-mode resonator operating at ∼1.34 MHz with a measured Q of 19 000 and a TCF of $+5$ ppm/°C at room temperature. This resonator has a turnover temperature of TCF at ∼90 °C, suitable for oscillator applications in ovenized platforms. Using compensation techniques, the frequency stability of these resonators is shown to be better than 110 ppb. The power handling limit was characterized to be -1 dBm, significantly better than their capacitive counterparts. These features make such resonators promising candidates for use in low-noise high-performance timing applications.

Future resonator designs will target lower motional impedance with improved compensation algorithms for short- and long-term frequency drifts.

Appendix
Equation of Motion and Electrostatic Tuning of the IBAR

In order to simplify the analysis, the IBAR is assumed to be composed of four cantilevers each one-half the flange length.

Energy Terms:

1) Strain energy of the beam in bending

$$\mathrm{P.E}_B = \frac{1}{2}\int_0^L EI\left[\frac{\partial^2 u(x,t)}{\partial x^2}\right]^2 \cdot dx.$$

2) A cantilever with two tuning electrodes on either side forms two capacitors [refer to Fig. 2(a)]. For a given resonator displacement $u(x,t)$ from its mean position, the energy stored in capacitors $C1$ and $C2$ is

$$\mathrm{P.E}_{C1} = \frac{1}{2}\int_0^L \frac{\epsilon t V^2}{[d-u(x,t)]}\cdot dx$$

$$\mathrm{P.E}_{C2} = \frac{1}{2}\int_0^L \frac{\epsilon t V^2}{[d+u(x,t)]}\cdot dx.$$

3) Kinetic energy of the beam in bending

$$\mathrm{K.E}_B = \frac{1}{2}\int_0^L \rho A\cdot\left[\frac{\partial u(x,t)}{\partial t}\right]^2 \cdot dx.$$

Form Equation of Motion Using Hamilton's Principle [27]: Form Lagrangian $L = \mathrm{K.E} - \mathrm{P.E}$.

From the principle of virtual work

$$\int_0^t \delta(L)\cdot dt = 0.$$

By substituting the energy terms in the above, integrating by parts twice, and rearranging terms, we get the equation of motion as

$$EI\frac{\partial^4 u(x,t)}{\partial x^4} + \rho A\frac{\partial^2 u(x,t)}{\partial t^2} - \frac{2\epsilon t V^2}{d^3}\cdot u(x,t) = 0.$$

Solution: The above equation can be solved using standard techniques [28], assuming that separation of variables is applicable, and using

$$\beta^4 = \frac{1}{EI}\left[\rho A\omega^2 + \frac{2\epsilon t V^2}{d^3}\right].$$

Then, the equation can be rewritten as

$$U''''(x) = \beta^4\cdot U(x).$$

By using the appropriate boundary conditions for a cantilever, we have the frequency relation as

$$\cos(\beta l)\cdot\cosh(\beta l) + 1 = 0.$$

Multiple solutions exist, and the first two are noted as follows:

$$z_1 = \beta_1 l = 1.875104$$
$$z_2 = \beta_2 l = 4.694091.$$

Here, $l = L/2$.

Since we are interested in the first mode, we will use z_1 in our further calculations. Thus, for the in-plane flexural mode, we can write the resonator frequency as

$$f = \frac{1}{2\pi}\cdot\sqrt[2]{\left[\frac{4}{3}\frac{E}{\rho}w^2\cdot\frac{z_1^4}{L^4} - 2\frac{\epsilon}{\rho}\cdot\frac{1}{w\cdot d^3}\cdot V^2\right]}.$$

For the given geometry and to enable direct comparison with measurements, certain tuning factors (n_1 and n_2) are explicitly added to give (2)

$$f = \frac{1}{2\pi}\cdot\sqrt[2]{\left[\frac{4}{3}\frac{E}{\rho}w^2\cdot\frac{z_1^4}{L^4} - n_1\frac{n_2}{8}\frac{\epsilon}{\rho}\cdot\frac{1}{w\cdot d^3}\cdot V^2\right]}$$

where E is the effective Young modulus of the resonator stack, ρ is the effective density of the resonator stack, w is the width of the IBAR side flange, L is the length of the IBAR side flange, d is the electrostatic gap between the flanges and the tuning electrodes ($d \sim 2$ μm in this process), t is the thickness of the silicon device layer ($\mathrm{IBAR\ thickness} = 20$ μm), ϵ is the dielectric constant for air, V is the applied tuning potential, n_1 is the ratio of tuning electrode length to beam length (L_e/L) ($\max = 1$), and n_2 is the number of electrodes used for tuning (out of a maximum of eight). All parameters are in SI units.

Equation (1) is simply extracted by taking $V = 0$ and is the standard equation for a cantilever resonating in its first-order flexural mode.

Acknowledgment

The authors would like to thank Y. Shim and V. Gokhale, both at the University of Michigan, Ann Arbor, MI, USA, for the helpful discussions. The authors would also like to thank the staff at the Lurie Nanofabrication Facility, University of Michigan, Ann Arbor, MI, USA, for their help with the device fabrication.

References

[1] C. T. C. Nguyen, "MEMS technology for timing and frequency control," *IEEE Trans. Ultrason., Ferroelectr., Freq. Control*, vol. 54, no. 2, pp. 251–270, Feb. 2007.

[2] F. Ayazi, "MEMS for integrated timing and spectral processing," in *Proc. IEEE Custom Integr. Circuits Conf.*, Sep. 13–16, 2009, pp. 65–72.

[3] S. Bhave, "Micro- (and nano-) mechanical signal processors," in *Proc. SPIE, Nano-Electron. High-Freq. MEMS/NEMS*, Orlando, FL, USA, Apr. 5, 2010, vol. 7679, pp. 76790J-1–76790J-6.
[4] "SiTime Enters $350M Voltage Controlled Oscillator (VCXO) Market with Industry's First MEMS-Based Device," Internet, Nov. 18, 2012. [Online]. Available: www.sitime.com
[5] "Discera's Low Power Oscillators Deliver Industry Best Reliability Rating and Widest Operating Range," Internet, Nov. 18, 2012. [Online]. Available: www.discera.com
[6] "IDT Introduces World's First Piezoelectric MEMS Oscillators for High-performance Applications," Internet, Nov. 18, 2012. [Online]. Available: www.idt.com
[7] G. Piazza, R. Abdolvand, G. Ho, and F. Ayazi, "Piezoelectrically-transduced, capacitively-tuned, high-Q single-crystal silicon micromechanical resonators on SOI wafers," *Sens. Actuators A, Phys.*, vol. 111, no. 1, pp. 71–78, Mar. 2004.
[8] M. Rinaldi, C. Zuo, J. Vander Spiegel, and G. Piazza, "Reconfigurable CMOS oscillator based on multifrequency AlN contour-mode MEMS resonators," *IEEE Trans. Electron Devices*, vol. 58, no. 5, pp. 1281–1286, May 2011.
[9] T. Cheng and S. Bhave, "High-Q, low impedance polysilicon resonators with 10 nm air gaps," in *Proc. 23rd IEEE Int. Conf. MEMS*, Hong Kong, Jan. 24–28, 2010, pp. 695–698.
[10] W.-T. Hsu, "Recent progress in silicon MEMS oscillators," in *Proc. 40th Annu. PTTI*, Reston, VA, USA, Dec. 2–4, 2008, pp. 135–146.
[11] B. Kim, R. Melamud, R. A. Candler, M. A. Hopcroft, C. M. Jha, S. Chandorkar, and T. Kenny, "Encapsulated MEMS resonators—A technology path for MEMS into frequency control applications," in *Proc. IEEE IFCS*, 2010, pp. 1–4.
[12] A. K. Samarao and F. Ayazi, "Temperature compensation of silicon resonators via degenerate doping," *IEEE Trans. Electron Devices*, vol. 59, no. 1, pp. 87–93, Jan. 2012.
[13] R. Melamud, B. Kim, S. Chandorkar, M. A. Hopcroft, M. Agarwal, C. M. Jha, and T. Kenny, "Temperature-compensated high-stability silicon resonators," *Appl. Phys. Lett.*, vol. 90, no. 24, pp. 244107-1–244107-3, Jun. 2007.
[14] R. Tabrizian, G. Casinovi, and F. Ayazi, "Temperature-stable high-Q AlN-on-silicon resonators with embedded array of oxide pillars," in *Proc. Solid-State Sens., Actuators, Microsyst. Workshop*, Hilton Head Island, SC, USA, Jun. 2010, pp. 100–101.
[15] M. Allah, J. Kaitila, R. Thalhammer, W. Weber, and D. Schmitt-Landseidel, "Temperature compensated solidly mounted bulk acoustic wave resonators with optimum piezoelectric coupling coefficient," in *IEDM Tech. Dig.*, Dec. 7–9, 2009, pp. 1–4.
[16] A. Rahafrooz and S. Pourkamali, "Fabrication and characterization of thermally actuated micromechanical resonators for airborne particle mass sensing, part I: Resonator design and modeling," *J. Micromech. Microeng.*, vol. 20, no. 12, pp. 125018-1–125018-10, Dec. 2010.
[17] A. Hajjam, J. C. Wilson, A. Rahafrooz, and S. Pourkamali, "Fabrication and characterization of thermally actuated micromechanical resonators for airborne particle mass sensing, part II: Device fabrication and characterization," *J. Micromech. Microeng.*, vol. 20, no. 12, p. 125019, Dec. 2010.
[18] H. Nathanson, W. Newell, R. Wickstrom, and J. Davis, Jr., "The resonant gate transistor," *IEEE Trans. Electron Devices*, vol. ED-14, no. 3, pp. 117–133, Mar. 1967.
[19] Product discontinued but refurbished equipment can be purchased online, Dec. 8, 2012. [Online]. Available: http://www.caeonline.com/listing/product/161343/ipec-westech-speedfam-avanti-472; For process details refer-Internet. [Online]. Available: http://ssel-sched.eecs.umich.edu/wiki/Public.CMP%20IPEC-472.ashx
[20] G. K. Ho, K. Sundaresan, S. Pourkamali, and F. Ayazi, "Micromechanical IBARs: Tunable high-Q resonators for temperature-compensated reference oscillators," *J. Microelectromech. Syst.*, vol. 19, no. 3, pp. 503–515, Jun. 2010.
[21] G. K. Ho, J. K. C. Perng, and F. Ayazi, "Micromechanical IBARs: Modeling and process compensation," *J. Microelectromech. Syst.*, vol. 19, no. 3, pp. 516–525, Jun. 2010.
[22] D. S. Bindel and S. Govindjee, "Elastic PMLs for resonator anchor loss simulation," *Int. J. Numer. Methods Eng.*, vol. 64, no. 6, pp. 789–818, Oct. 2005.
[23] "Thermoelastic Damping in a MEMS Resonator," Internet, Nov. 18, 2012. [Online]. Available: http://www.comsol.com/showroom/gallery/1439/
[24] R. Abdolvand, H. Johari, G. K. Ho, A. Erbil, and F. Ayazi, "Quality factor in trench-refilled polysilicon beam resonators," *J. Microelectromech. Syst.*, vol. 15, no. 3, pp. 471–478, Jun. 2006.
[25] Date of access Dec. 2012. [Online]. Available: http://www.ni.com/labview/
[26] R. Tabrizian and F. Ayazi, "Laterally excited silicon bulk acoustic resonator with sidewall AlN," in *Proc. TRANSDUCERS*, Beijing, China, Jun. 2011, pp. 1520–1523.
[27] Y. C. Fung and P. Tong, "Hamilton's principle, wave propagation, applications of generalized coordinates," in *Classical and Computational Solid Mechanics*. Singapore: World Scientific, 2001.
[28] K. F. Graff, "Flexural waves in thin rods," in *Wave Motion in Elastic Solids*. Columbus, OH, USA: Ohio State Univ. Press, 1975.

Vikram A. Thakar (S'12) received the B.E. degree in mechanical engineering from the University of Pune, Pune, India, in 2006 and the M.E. degree in integrated microsystems from the University of Michigan, Ann Arbor, MI, USA, in 2011, where he is currently working toward the Ph.D. degree in the Department of Mechanical Engineering.

His research interests are in the areas of resonant micromechanical devices, acoustically coupled micromechanical resonators, and piezoelectrically actuated resonators for oscillator applications. The main focus of his research is on the relation between device modeling and fabrication as it applies in the MEMS domain.

Zhengzheng Wu (S'09) received the B.S. degree in microelectronics from Fudan University, Shanghai, China, in 2005 and the M.S. degree in microelectronics from the Shanghai Institute of Microsystem and Information Technology, Chinese Academy of Sciences, Shanghai, in 2009. He is currently working toward the Ph.D. degree in the Department of Electrical Engineering and Computer Science, University of Michigan, Ann Arbor, MI, USA.

During the summer of 2011, he was an Intern with Samsung Telecommunications America, Dallas, TX, USA, where he was involved in developing multiband RF power amplifiers for wireless handsets. His research interests include MEMS for wireless applications and timing references, tunable RF filters and passive circuits, circuits for wireless transceivers, and integrated microsystems.

Mr. Wu was the recipient of the Rackham International Student Fellowship from the University of Michigan, Ann Arbor, MI, USA, for 2010–2011.

Adam Peczalski (S'12) received the B.S. degree in electrical engineering from the University of Wisconsin, Madison, WI, USA, in 2011. He is currently working toward the Ph.D. degree in the Department of Electrical Engineering and Computer Science, University of Michigan, Ann Arbor, MI, USA.

His research interests include MEMS–CMOS integration, MEMS fabrication techniques, and MEMS resonators. He is currently investigating the use of silica as a mechanical material for resonators.

Mina Rais-Zadeh (S'03–M'08–SM'12) received the B.S. degree in electrical engineering from Sharif University of Technology, Tehran, Iran, and the M.S. and Ph.D. degrees in electrical and computer engineering from the Georgia Institute of Technology, Atlanta, GA, USA, in 2005 and 2008, respectively.

From August 2008 to 2009, she was a Postdoctoral Research Fellow with the Integrated MEMS Group, Georgia Institute of Technology. Since January 2009, she has been with the University of Michigan, Ann Arbor, MI, USA, where she is currently an Assistant Professor with the Department of Electrical Engineering and Computer Science. Her research interests include passive micromachined devices for communication applications, resonant micromechanical devices, gallium nitride MEMS, and micro-/nanofabrication process development.

Prof. Rais-Zadeh was the recipient of the NASA Early Career Faculty Award (2012), the NSF CAREER Award (2011), and the IEEE Electron Devices Society Early Career Award (2011) and was a finalist in the student paper competitions at the Silicon Monolithic Integrated Circuits in RF Systems (2007) and International Microwave Symposium (2011) conferences. She serves as a Member of the Technical Program Committee of the IEEE International Electron Devices Meeting, IEEE Sensors, and the Hilton Head Workshop.